Input-Constrained Hybrid Control of a Hyper-Redundant Mobile Medical Manipulator

ZHANG Kaibo[1] (张凯波),　CHEN Li[1*] (陈　丽),　DONG Qi[2] (董　琦)

(1. School of Air Transportation, Shanghai University of Engineering Science, Shanghai 201620, China;
2. Function Teaching and Research Office, Mudanjiang Medical University, Mudanjiang 157011, Heilongjiang, China)

Abstract: To reduce the risk of infection in medical personnel working in infectious-disease areas, we proposed a hyper-redundant mobile medical manipulator (HRMMM) to perform contact tasks in place of healthcare workers. A kinematics-based tracking algorithm was designed to obtain highly accurate pose tracking. A kinematic model of the HRMMM was established and its global Jacobian matrix was deduced. An expression of the tracking error based on the Rodrigues rotation formula was designed, and the relationship between tracking errors and gripper velocities was derived to ensure accurate object tracking. Considering the input constraints of the physical system, a joint-constraint model of the HRMMM was established, and the variable-substitution method was used to transform asymmetric constraints to symmetric constraints. All constraints were normalized by dividing by their maximum values. A hybrid controller based on pseudo-inverse (PI) and quadratic programming (QP) was designed to satisfy the real-time motion-control requirements in medical events. The PI method was used when there was no input saturation, and the QP method was used when saturation occurred. A quadratic performance index was designed to ensure smooth switching between PI and QP. The simulation results showed that the HRMMM could approach the target pose with a smooth motion trajectory, while meeting different types of input constraints.

Key words: input-constrained hybrid control, hyper-redundant mobile medical manipulator (HRMMM), pseudo-inverse (PI), quadratic programming (QP), pose tracking

CLC number: TP 242　　**Document code:** A

Nomenclature

$\boldsymbol{D}$— Normalized matrix
$\boldsymbol{e}$— Pose error
$\hat{\boldsymbol{e}}$— Joint position error
$\boldsymbol{f}$— Coefficient vector
$\boldsymbol{H}$— Coefficient matrix
$\boldsymbol{J}$— Global Jacobian matrix
$\boldsymbol{J}_{\mathrm{o}}$— Jacobian matrix of the lifting manipulator
$\boldsymbol{L}_{\mathrm{P}}$— Pose-error interaction matrix
$\boldsymbol{L}_{\mathrm{R}}$— Rotating interaction matrix
$\boldsymbol{p}_{\mathrm{e}}$— Initial gripper pose
$\boldsymbol{p}_{*\mathrm{e}}$— Target gripper pose
(p_x, p_y, p_z)— Gripper position
$\boldsymbol{q}$— Joint position vector
$\boldsymbol{q}_0$— Joint position vector at the previous moment

$\dot{\boldsymbol{q}}$— Joint velocity vector
$\dot{\bar{\boldsymbol{q}}}$— Joint velocity vector with variable substitution
$\boldsymbol{R}$— Rotation matrix
$\boldsymbol{t}$— Position vector
$\boldsymbol{T}$— Homogeneous transformation matrix
$\boldsymbol{U}_{\mathrm{o}}$— Normalized double-ended constraint
v— Linear velocity
$\boldsymbol{V}_{\mathrm{e}}$— Gripper velocity in the gripper coordinate system
$\boldsymbol{V}_{\mathrm{g}}$— Gripper velocity in the world coordinate system
α— Heading angle
$\boldsymbol{\zeta}$— State of the mobile platform
θ— Joint angle
$\theta\boldsymbol{u}$— Rotation vector
$\boldsymbol{\xi}$— Double-ended constraint
(ϕ_x, ϕ_y, ϕ_z)— Gripper attitude
ω— Angular velocity

0　Introduction

Medical robots are robots used for medical treatment or auxiliary medical care in medical scenarios. Medical robots can be divided into four categories: surgical robots[1], rehabilitation robots[2], auxiliary robots[3],

and service robots[4].

A mobile manipulator is an example of an auxiliary robot. It includes a mobile platform and a manipulator. The platform is capable of large-scale movement and the manipulator can conduct delicate operations. An important development trend in medical robots is that the mobile manipulator greatly improves the working range and flexibility of the manipulator[5].

The problem of coordinating the mobile-platform control and manipulator control is caused by an increase in the degrees of freedom (DOFs) of the mobile manipulator. The current solution to this problem has two branches: decentralized coordinated control and integral control[6-7]. Decentralized coordinated control refers to separately controlling the motions of the manipulator and mobile platform. The motion between the manipulator and mobile platform must conform to the physical connection. Current research methods include virtual vehicle[8], preferred manipulator configuration[9], zero-moment point[10], and segmented-motion planning[11].

In integral control, the manipulator and mobile platform are controlled as a whole with high DOFs. In general, the global Jacobian matrix of the mobile manipulator is first established, followed by a global kinematic and dynamic model[12-13]. The decentralized control method simplifies the system design but limits the overall high-DOF motion capability of the system. The integral control method can establish a comprehensive index to optimize the system as a whole; however, it requires extensive calculations because of the large number of DOFs[14].

The traditional inverse-kinematic methods of redundant manipulators include Jacobian matrix transformation, pseudo-inverse (PI), and damped least-squares[15]. In practical applications, the physical input constraints of the system must be considered in inverse kinematics, including the position and velocity constraints of the joints.

A redundant manipulator uses the redundant characteristics of the system to prevent the joint from reaching its limit. The main methods are as follows: gradient projection[16], weighted least-norm (WLN)[17-18], quadratic programming (QP)[19-20], flexible-priority solution[21], prediction[22], and null-space saturation[23]. The above studies are all oriented to the same type of rotating-joint manipulator system, and the inverse kinematics is solved within the symmetric physical constraints of the joint position and velocity.

Existing inverse-kinematic algorithms for mobile manipulators are mainly based on a direct application or extension of the above methods[24-25]. However, considering the mobile manipulator as a complete system, it has asymmetric input constraints, including positive linear velocities, a one-way lift-device displacement, and asymmetric limits of joint velocities. An advanced

optimal algorithm can be used to deduce the asymmetric constraints at the cost of complex calculations[26-27]. Therefore, it is difficult to achieve real-time target-tracking control.

In this study, the kinematic equations of the manipulator and mobile platform as a whole were established, and the global Jacobian matrix of a hyper-redundant mobile medical manipulator (HRMMM) was derived. A physical-constraint model of the system was established and the asymmetric physical constraints were converted to symmetric. Thus, the standard QP could be implemented to quickly solve the inverse kinematics. Moreover, the symmetrized constraint variables were normalized to unify the optimal function of the joint variables for the QP solution. Then, a hybrid control scheme based on PI and standard QP was proposed to realize real-time target-pose tracking control within the physical constraints.

1 Kinematics of HRMMM

1.1 Parameters of HRMMM

The HRMMM is composed of a two-wheeled differential mobile platform (IR-C100), a lifting platform (lifting rod and holder), and a 7-DOF Gen3 manipulator (Kinova). Thus, the entire system has 10 DOFs, as shown in Fig. 1. The structural parameters of the manipulator can be found in the Gen3 user guide[①], which includes the link length d_i and joint offset a_i.

1.2 Kinematics of Lifting Manipulator

The established coordinate systems for the HRMMM are shown in Fig. 1. The lifting platform drives the manipulator up and down, and the lifting platform and manipulator can be combined into an 8-DOF lifting manipulator. In addition, the coordinate system $o^s y^s z^s$ is denoted as {s}, and so on. The kinematic model of the system is established as follows.

The transformation matrix between the coordinate systems {s} and {a} is as follows:

$$ {}_{a}^{s}\boldsymbol{T} = \begin{bmatrix} 1 & 0 & 0 & 0 \\ 0 & 1 & 0 & 0 \\ 0 & 0 & 1 & d \\ 0 & 0 & 0 & 1 \end{bmatrix}. \tag{1} $$

The transformation matrix between the coordinate systems {a} and {1} is as follows:

$$ {}_{1}^{a}\boldsymbol{T} = \begin{bmatrix} \cos\theta_1 & -\sin\theta_1 & 0 & 0 \\ -\sin\theta_1 & -\cos\theta_1 & 0 & 0 \\ 0 & 0 & -1 & d_{a} \\ 0 & 0 & 0 & 1 \end{bmatrix}. \tag{2} $$
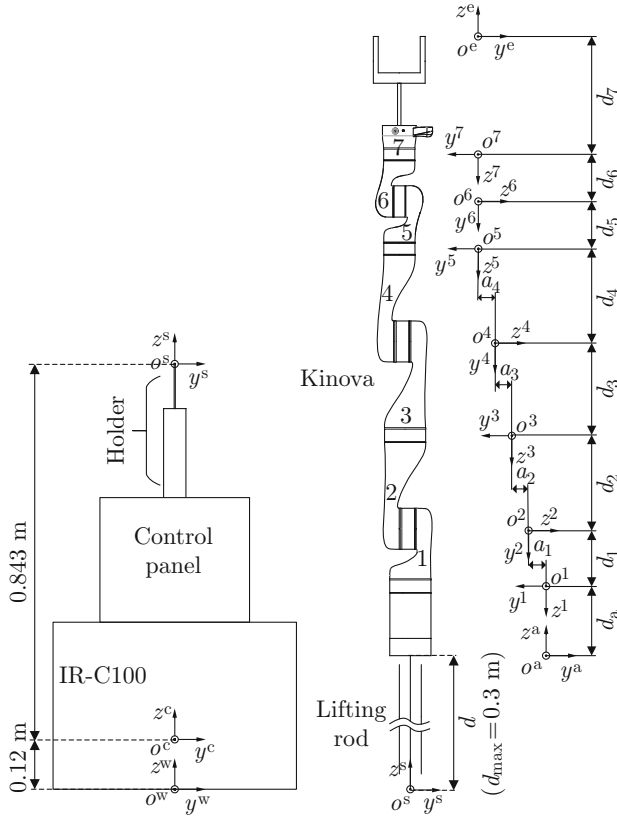
Fig. 1   Structure of the HRMMM

The transformation matrix $_i^{i-1}\boldsymbol{T}$ between the coordinate systems of each link i of the manipulator is related to the link parity. When the link i is even,

$$_i^{i-1}\boldsymbol{T} = \begin{bmatrix} \cos\theta_i & -\sin\theta_i & 0 & 0 \\ 0 & 0 & -1 & a_{i-1} \\ \sin\theta_i & \cos\theta_i & 0 & -d_{i-1} \\ 0 & 0 & 0 & 1 \end{bmatrix}. \quad (3)$$

When the link i is odd,

$$_i^{i-1}\boldsymbol{T} = \begin{bmatrix} \cos\theta_i & -\sin\theta_i & 0 & 0 \\ 0 & 0 & 1 & -d_{i-1} \\ -\sin\theta_i & -\cos\theta_3 & 0 & -a_{i-1} \\ 0 & 0 & 0 & 1 \end{bmatrix}. \quad (4)$$

The transformation matrix between the coordinate systems {7} and {e} is as follows:

$$_e^7\boldsymbol{T} = \begin{bmatrix} 1 & 0 & 0 & 0 \\ 0 & -1 & 0 & 0 \\ 0 & 0 & -1 & -d_7 \\ 0 & 0 & 0 & 1 \end{bmatrix}. \quad (5)$$

By multiplying the transformation matrix obtained above, the transformation matrix $_i^s\boldsymbol{T}$ of the joint co-

ordinate system {i}, relative to the lifting-platform coordinate system {s}, is as follows:

$$_i^s\boldsymbol{T} = \begin{bmatrix} \boldsymbol{n}_i & \boldsymbol{o}_i & \boldsymbol{a}_i & \boldsymbol{t}_i \\ 0 & 0 & 0 & 1 \end{bmatrix} = \\ _a^s\boldsymbol{T}\,_1^a\boldsymbol{T}\,_2^1\boldsymbol{T}\cdots\,_{i-1}^{i-2}\boldsymbol{T}\,_i^{i-1}\boldsymbol{T}. \quad (6)$$

1.3   Global Jacobian Matrix

The state of the mobile platform is $\boldsymbol{\zeta} = (x_0, y_0, \alpha)^{\mathrm{T}}$, where (x_0, y_0) is the position of the mobile platform in the world coordinate system and α is the heading angle, as shown in Fig. 2. In addition, v_c and ω_c are defined as the linear and angular velocities of the mobile platform in the world coordinate system, respectively. Assuming that the contact motion between the driving wheel of the mobile platform and the ground is purely rolling, the motion equation is as follows:

$$\dot{\boldsymbol{\zeta}} = \begin{bmatrix} \dot{x}_0 \\ \dot{y}_0 \\ \dot{\alpha} \end{bmatrix} = \begin{bmatrix} \cos\alpha & 0 \\ \sin\alpha & 0 \\ 0 & 1 \end{bmatrix} \begin{bmatrix} v_c \\ \omega_c \end{bmatrix}. \quad (7)$$
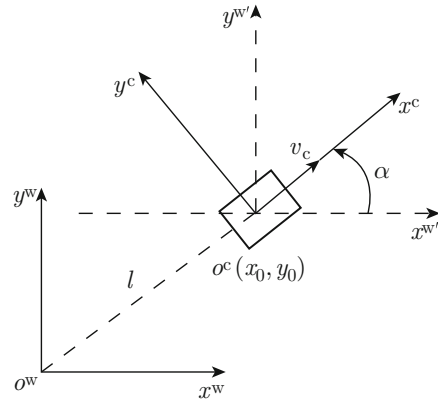

Fig. 2   Kinematic model of the mobile platform

The Jacobian matrix of the 8-DOF lifting manipulator is represented by the following vector-product construction method:

$$\boldsymbol{J}_o = \begin{bmatrix} \boldsymbol{a}_a & \boldsymbol{a}_1 \times \boldsymbol{r}_1 & \cdots & \boldsymbol{a}_6 \times \boldsymbol{r}_6 & \boldsymbol{a}_7 \times \boldsymbol{r}_7 \\ \boldsymbol{0} & \boldsymbol{a}_1 & \cdots & \boldsymbol{a}_6 & \boldsymbol{a}_7 \end{bmatrix}, \quad (8)$$

where, $\boldsymbol{r}_i = \boldsymbol{t}_e - \boldsymbol{t}_i$ represents the displacement vector between the origin of the gripper coordinate system {e} and the origin of the joint coordinate system {i}; $\boldsymbol{a}_i$ and $\boldsymbol{t}_i$ can be obtained from Eq. (6).

If the position of the gripper in the coordinate system {s} is $(p_x^s, p_y^s, p_z^s)^{\mathrm{T}}$, its position in the mobile-platform coordinate system {c} is $(p_x^c, p_y^c, p_z^c)^{\mathrm{T}}$, where $(p_x^c, p_y^c, p_z^c)^{\mathrm{T}} = (p_x^s, p_y^s, p_z^s + 0.843)^{\mathrm{T}}$. Thus, its position

in the world coordinate system {w} can be expressed as follows:

$$\begin{bmatrix} p_x^{\mathrm{w}} \\ p_y^{\mathrm{w}} \\ p_z^{\mathrm{w}} \end{bmatrix} = \begin{bmatrix} \cos\alpha & -\sin\alpha & 0 \\ \sin\alpha & \cos\alpha & 0 \\ 0 & 0 & 1 \end{bmatrix} \begin{bmatrix} p_x^{\mathrm{s}} \\ p_y^{\mathrm{s}} \\ p_z^{\mathrm{s}} \end{bmatrix} + \begin{bmatrix} x_0 \\ y_0 \\ l_{\mathrm{o}} \end{bmatrix}, \quad (9)$$

where $l_{\mathrm{o}} = 0.12\,\mathrm{m}$ is the distance between the origin of {c} and that of {w}, as shown in Fig. 1.

The transformation relationship between the velocity of the gripper in the world coordinate system and that in the base coordinate system can be obtained by deriving Eq. (9), as follows:

$$\begin{bmatrix} \dot{p}_x^{\mathrm{w}} \\ \dot{p}_y^{\mathrm{w}} \\ \dot{p}_z^{\mathrm{w}} \end{bmatrix} = \begin{bmatrix} -\dot{\alpha}\sin\alpha & -\dot{\alpha}\cos\alpha & 0 \\ \dot{\alpha}\cos\alpha & -\dot{\alpha}\sin\alpha & 0 \\ 0 & 0 & 1 \end{bmatrix} \begin{bmatrix} p_x^{\mathrm{s}} \\ p_y^{\mathrm{s}} \\ p_z^{\mathrm{s}} \end{bmatrix} + $$
$$\begin{bmatrix} \cos\alpha & -\sin\alpha & 0 \\ \sin\alpha & \cos\alpha & 0 \\ 0 & 0 & 1 \end{bmatrix} \begin{bmatrix} \dot{p}_x^{\mathrm{s}} \\ \dot{p}_y^{\mathrm{s}} \\ \dot{p}_z^{\mathrm{s}} \end{bmatrix} + \begin{bmatrix} \dot{x}_0 \\ \dot{y}_0 \\ 0 \end{bmatrix}. \quad (10)$$

Similarly, the relationship between the gripper angular velocity $(\dot{\phi}_x^{\mathrm{w}}, \dot{\phi}_y^{\mathrm{w}}, \dot{\phi}_z^{\mathrm{w}})^{\mathrm{T}}$ in the world coordinate system and $(\dot{\phi}_x^{\mathrm{s}}, \dot{\phi}_y^{\mathrm{s}}, \dot{\phi}_z^{\mathrm{s}})^{\mathrm{T}}$ in the base coordinate system is

$$\begin{bmatrix} \dot{\phi}_x^{\mathrm{w}} \\ \dot{\phi}_y^{\mathrm{w}} \\ \dot{\phi}_z^{\mathrm{w}} \end{bmatrix} = \begin{bmatrix} \cos\alpha & -\sin\alpha & 0 \\ \sin\alpha & \cos\alpha & 0 \\ 0 & 0 & 1 \end{bmatrix} \begin{bmatrix} \dot{\phi}_x^{\mathrm{s}} \\ \dot{\phi}_y^{\mathrm{s}} \\ \dot{\phi}_z^{\mathrm{s}} \end{bmatrix} + \begin{bmatrix} 0 \\ 0 \\ \dot{\alpha} \end{bmatrix}. \quad (11)$$

By combining Eqs. (7)—(11), when $T_1 = \cos\alpha$, $T_2 = -p_x^{\mathrm{s}}\sin\alpha - p_y^{\mathrm{s}}\cos\alpha$, $T_3 = \sin\alpha$, and $T_4 = p_x^{\mathrm{s}}\cos\alpha - p_y^{\mathrm{s}}\sin\alpha$, the gripper velocity in the world coordinate system is defined as $\boldsymbol{V}_{\mathrm{g}} = (\dot{p}_x^{\mathrm{w}}, \dot{p}_y^{\mathrm{w}}, \dot{p}_z^{\mathrm{w}}, \dot{\phi}_x^{\mathrm{w}}, \dot{\phi}_y^{\mathrm{w}}, \dot{\phi}_z^{\mathrm{w}})^{\mathrm{T}}$, the general joint-velocity vector of the HRMMM $\dot{\boldsymbol{q}} = (v_{\mathrm{c}}, \omega_{\mathrm{c}}, \dot{d}, \dot{\theta}_1, \dot{\theta}_2, \cdots, \dot{\theta}_7)^{\mathrm{T}}$, and the following can be obtained:

$$\boldsymbol{V}_{\mathrm{g}} = \boldsymbol{J}\dot{\boldsymbol{q}}. \quad (12)$$

The global Jacobian matrix is as follows:

$$\boldsymbol{J} = \begin{bmatrix} T_1 & T_2 & & & \\ T_3 & T_4 & & & \\ 0 & 0 & \boldsymbol{R}_z & \boldsymbol{0}_{(3\times3)} & \\ 0 & 0 & \boldsymbol{0}_{(3\times3)} & \boldsymbol{R}_z & \\ 0 & 0 & & & \\ 0 & 1 & & & \end{bmatrix} \begin{bmatrix} \boldsymbol{I}_{(2\times2)} & \boldsymbol{0}_{(2\times8)} \\ \boldsymbol{0}_{(6\times2)} & \boldsymbol{J}_{\mathrm{o}(6\times8)} \end{bmatrix}, \quad (13)$$

where

$$\boldsymbol{R}_z = \begin{bmatrix} \cos\alpha & -\sin\alpha & 0 \\ \sin\alpha & \cos\alpha & 0 \\ 0 & 0 & 1 \end{bmatrix}. \quad (14)$$

2 Tracking-Controller Design

2.1 Pose-Tracking Strategy

The current and target poses of the gripper in the world coordinate system are $\boldsymbol{p}_{\mathrm{e}} = (p_x^{\mathrm{w}}, p_y^{\mathrm{w}}, p_z^{\mathrm{w}}, \phi_x^{\mathrm{w}}, \phi_y^{\mathrm{w}}, \phi_z^{\mathrm{w}})^{\mathrm{T}}$ and $\boldsymbol{p}_{*\mathrm{e}} = ({}^*p_x^{\mathrm{w}}, {}^*p_y^{\mathrm{w}}, {}^*p_z^{\mathrm{w}}, {}^*\phi_x^{\mathrm{w}}, {}^*\phi_y^{\mathrm{w}}, {}^*\phi_z^{\mathrm{w}})^{\mathrm{T}}$, respectively, as shown in Fig. 3. Assuming that the target pose is used for grasping, the transformation matrices of the current pose $\boldsymbol{p}_{\mathrm{e}}$ and target pose $\boldsymbol{p}_{*\mathrm{e}}$ within the world coordinate system are ${}_{\mathrm{e}}^{\mathrm{w}}\boldsymbol{T}$ and ${}_{*\mathrm{e}}^{\mathrm{w}}\boldsymbol{T}$, respectively. Then, the transformation matrix of the target pose to the current pose ${}_{*\mathrm{e}}^{\mathrm{e}}\boldsymbol{T}$ is obtained, and the position vector ${}_{*\mathrm{e}}^{\mathrm{e}}\boldsymbol{t}$ and rotation matrix ${}_{*\mathrm{e}}^{\mathrm{e}}\boldsymbol{R}$ are extracted from ${}_{*\mathrm{e}}^{\mathrm{e}}\boldsymbol{T}$.
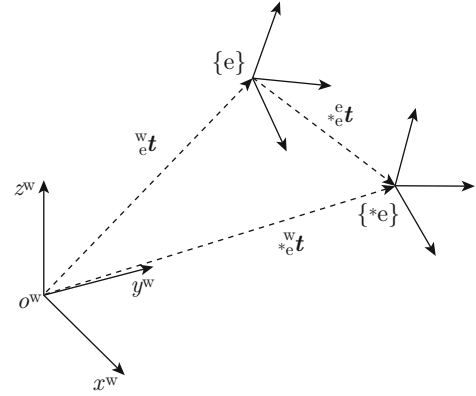

Fig. 3　Current and target poses of the gripper

The control objective is to make the gripper's current pose $\boldsymbol{p}_{\mathrm{e}}$ consistent with the target grasping pose $\boldsymbol{p}_{*\mathrm{e}}$; that is, ${}_{*\mathrm{e}}^{\mathrm{e}}\boldsymbol{t}$ approaches the zero vector and ${}_{*\mathrm{e}}^{\mathrm{e}}\boldsymbol{R}$ approaches the unit matrix.

To simplify the number of variables, the Rodrigues equivalent rotation vector $\theta\boldsymbol{u} = (r_x, r_y, r_z)^{\mathrm{T}}$ is used to represent the rotation transformation ${}_{*\mathrm{e}}^{\mathrm{e}}\boldsymbol{R}$. The norm of $(r_x, r_y, r_z)^{\mathrm{T}}$ represents the size of the equivalent rotation angle and the unit vector of $(r_x, r_y, r_z)^{\mathrm{T}}$ represents the equivalent rotation axis $\boldsymbol{u}$. The conversion between the equivalent rotation vector $\theta\boldsymbol{u}$ and the rotation matrix $\boldsymbol{R}$ can be obtained using the following Rodrigues rotation formula[28]:

$$\left.\begin{array}{c} \boldsymbol{R} = \begin{bmatrix} r_{11} & r_{12} & r_{13} \\ r_{21} & r_{22} & r_{23} \\ r_{31} & r_{32} & r_{33} \end{bmatrix} \\[6pt] \theta = \arccos\dfrac{\mathrm{tr}(\boldsymbol{R}) - 1}{2} \\[6pt] \boldsymbol{u} = \dfrac{1}{2\sin\theta} \begin{bmatrix} r_{32} - r_{23} \\ r_{13} - r_{31} \\ r_{21} - r_{12} \end{bmatrix} \end{array}\right\}. \quad (15)$$

Therefore, the error between the current and target poses of the gripper can be expressed as $\boldsymbol{e} = ({}_{*\mathrm{e}}^{\mathrm{e}}\boldsymbol{t}, \theta\boldsymbol{u})^{\mathrm{T}}$,

and the control objective is $e \to 0$. Assuming that the velocities of the gripper in the world coordinate system and the current gripper coordinate system are $\boldsymbol{V}_{\mathrm{g}} = (v_{\mathrm{g}}, \omega_{\mathrm{g}})^{\mathrm{T}}$ and $\boldsymbol{V}_{\mathrm{e}} = (v_{\mathrm{e}}, \omega_{\mathrm{e}})^{\mathrm{T}}$, respectively,

$$\boldsymbol{V}_{\mathrm{e}} = \boldsymbol{L}_{\mathrm{R}} \boldsymbol{V}_{\mathrm{g}}, \tag{16}$$

where $\boldsymbol{L}_{\mathrm{R}}$ is a rotating interaction matrix expressed as follows:

$$\boldsymbol{L}_{\mathrm{R}} = \begin{bmatrix} {}_{\mathrm{e}}^{\mathrm{w}}\boldsymbol{R}^{\mathrm{T}} & \boldsymbol{0} \\ \boldsymbol{0} & {}_{\mathrm{e}}^{\mathrm{w}}\boldsymbol{R}^{\mathrm{T}} \end{bmatrix}. \tag{17}$$

Based on Fig. 3,

$$_{*\mathrm{e}}^{\mathrm{w}}\boldsymbol{t} = {}_{\mathrm{e}}^{\mathrm{w}}\boldsymbol{R}\,{}_{*\mathrm{e}}^{\mathrm{e}}\boldsymbol{t} + {}_{\mathrm{e}}^{\mathrm{w}}\boldsymbol{t}. \tag{18}$$

By taking the derivative of Eq. (18), the target position is fixed to the world coordinate system. Therefore, $_{*\mathrm{e}}^{\mathrm{w}}\dot{\boldsymbol{t}} = \boldsymbol{0}$ and ${}_{\mathrm{e}}^{\mathrm{w}}\dot{\boldsymbol{R}}\,{}_{*\mathrm{e}}^{\mathrm{e}}\boldsymbol{t} = {}_{\mathrm{e}}^{\mathrm{w}}\boldsymbol{R}\omega_{\mathrm{e}} \times {}_{*\mathrm{e}}^{\mathrm{e}}\boldsymbol{t}$;

$$_{\mathrm{e}}^{\mathrm{w}}\dot{\boldsymbol{t}} = {}_{\mathrm{e}}^{\mathrm{w}}\boldsymbol{R}(\omega_{\mathrm{e}} \times {}_{*\mathrm{e}}^{\mathrm{e}}\boldsymbol{t} + {}_{*\mathrm{e}}^{\mathrm{e}}\dot{\boldsymbol{t}}), \tag{19}$$

where ω_{e} denotes the instantaneous angular velocity of the gripper in the gripper coordinate system, and the following expression is obtained:

$$_{*\mathrm{e}}^{\mathrm{e}}\dot{\boldsymbol{t}} = -\boldsymbol{V}_{\mathrm{e}} - \omega_{\mathrm{e}} \times {}_{*\mathrm{e}}^{\mathrm{e}}\boldsymbol{t}. \tag{20}$$

Equation (20) provides the relationship between the derivative of the position error $_{*\mathrm{e}}^{\mathrm{e}}\boldsymbol{t}$ and $\boldsymbol{V}_{\mathrm{e}}$.

Similarly, taking the derivative of $\theta\boldsymbol{u}$ gives the following expression:

$$\frac{\mathrm{d}(\theta\boldsymbol{u})}{\mathrm{d}t} = \boldsymbol{L}_{\mathrm{w}}\omega_{\mathrm{e}}. \tag{21}$$

In Eq. (21), $\boldsymbol{L}_{\mathrm{w}}$ satisfies $\boldsymbol{L}_{\mathrm{w}}^{-1}\theta_{\mathrm{e}}\boldsymbol{u}_{\mathrm{e}} = \theta_{\mathrm{e}}\boldsymbol{u}_{\mathrm{e}}$ and can be obtained by[29]

$$\boldsymbol{L}_{\mathrm{w}} = \boldsymbol{I}_3 - \frac{\theta}{2}(\boldsymbol{u})_{\times} + \left(1 - \frac{\mathrm{sinc}(\theta)}{\mathrm{sinc}^2\left(\frac{\theta}{2}\right)}\right)(\boldsymbol{u})_{\times}^2, \tag{22}$$

where $(\boldsymbol{u})_{\times}$ represents the antisymmetric matrix of the rotation axis $\boldsymbol{u}$, and sinc is defined as

$$\mathrm{sinc}(\theta) = \begin{cases} \dfrac{\sin\theta}{\theta}, & \theta \neq 0 \\ 1, & \theta = 0 \end{cases}. \tag{23}$$

According to Eqs. (20) and (21), the relationship between $\boldsymbol{V}_{\mathrm{e}}$ and the derivative of the tracking error $\dot{\boldsymbol{e}}$ can be obtained as

$$\dot{\boldsymbol{e}} = \boldsymbol{L}_{\mathrm{p}}\boldsymbol{V}_{\mathrm{e}}, \tag{24}$$

where $\boldsymbol{L}_{\mathrm{p}}$ represents the pose-error interaction matrix, expressed as follows:

$$\boldsymbol{L}_{\mathrm{p}} = \begin{bmatrix} -\boldsymbol{I} & ({}_{*\mathrm{e}}^{\mathrm{e}}\boldsymbol{t})_{\times} \\ 0 & \boldsymbol{L}_{\mathrm{w}} \end{bmatrix}. \tag{25}$$

Assuming that the error is reduced exponentially and the derivative of the error satisfies $\dot{\boldsymbol{e}} = -k\boldsymbol{e}$, it is substituted into Eq. (24) to reach the target position as quickly as possible and expressed as follows:

$$\boldsymbol{V}_{\mathrm{e}} = -k\boldsymbol{L}_{\mathrm{p}}^{-1}\boldsymbol{e}. \tag{26}$$

Combined with Eq. (16), the tracking velocity of the gripper can be obtained as follows:

$$\boldsymbol{V}_{\mathrm{g}} = -k\boldsymbol{L}_{\mathrm{R}}^{-1}\boldsymbol{L}_{\mathrm{p}}^{-1}\boldsymbol{e}. \tag{27}$$

The logical block diagram of the entire control system is shown in Fig. 4. After the tracking velocity of the gripper $\boldsymbol{V}_{\mathrm{g}}$ is obtained, the inverse kinematics of the HRMMM system is calculated, and the velocity control variable $\dot{\boldsymbol{q}}$ of the system is obtained. The position-control variable $\boldsymbol{q}$ of the mobile manipulator is also obtained by integration, and the pose of the gripper ${}_{\mathrm{e}}^{\mathrm{s}}\boldsymbol{T}$ is obtained by the forward kinematics of the HRMMM. The pose matrix ${}_{\mathrm{e}}^{\mathrm{w}}\boldsymbol{T}$ relative to the world coordinate system was updated, and the pose error ${}_{*\mathrm{e}}^{\mathrm{e}}\boldsymbol{T}$ was obtained using the coordinate transformation matrix ${}_{*\mathrm{e}}^{\mathrm{w}}\boldsymbol{T}$ of the target.
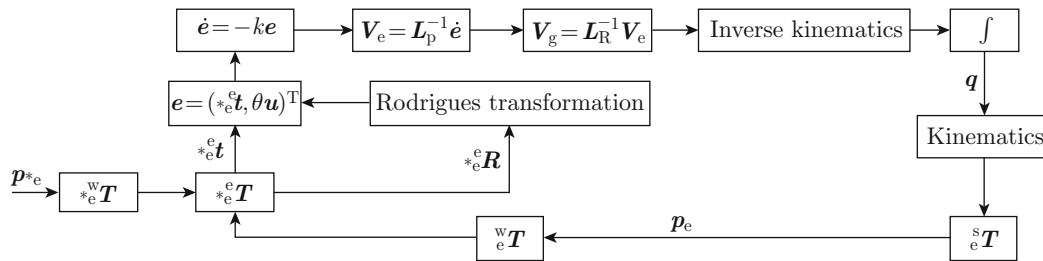

Fig. 4   Structure of the position-tracking guidance system

2.2   Physical-Constraint Model

The physical constraints of the HRMMM include the velocity constraints of the mobile platform, velocity and displacement constraints of the lifting platform, and position and velocity constraints of the manipulator joints. To expand the workspace of the medical manipulator,

the displacement and azimuth of the mobile platform were unlimited and replaced by $\pm\infty$ in the simulation.

The physical-constraint limits of the linear velocity v_c and angular velocity ω_c of the mobile platform were $\pm 2\,\mathrm{m/s}$ and $\pm 2\,\mathrm{rad/s}$, respectively. The displacement range of the lifting platform was 0—0.3 m and the physical limit of the lifting speed was $\pm 0.1\,\mathrm{m/s}$. The limits of each joint of the manipulator can be found in the Gen3 user guide.

The constraints have different dimensions (angle and distance), levels (position and velocity), and asymmetry. For the integral-controller design of the HRMMM system, the physical constraints must be symmetrized and normalized to establish a unified optimization performance index, and a simple optimization algorithm must be adopted to solve the inverse kinematics.

2.2.1 Position-Constraint Transformation

The system kinematic model in Eq. (12) was solved at the velocity level. Therefore, the position constraint was transferred to the velocity level for consideration. For example, a generalized position variable $\boldsymbol{q} = (l, \alpha, d, \theta_1, \theta_2, \cdots, \theta_7)^{\mathrm{T}}$ is defined, where $l = \sqrt{x_0^2 + y_0^2}$ is the distance between the mobile platform and the initial position. During movement, the position limit can be expressed as follows:

$$\boldsymbol{q}_{\min} \leqslant \boldsymbol{q} + \dot{\boldsymbol{q}}\Delta t \leqslant \boldsymbol{q}_{\max}, \tag{28}$$

where Δt denotes the control period. Using $\mu = 1/\Delta t$, the above equation can be rewritten as follows:

$$\mu(\boldsymbol{q}_{\min} - \boldsymbol{q}) \leqslant \dot{\boldsymbol{q}} \leqslant \mu(\boldsymbol{q}_{\max} - \boldsymbol{q}). \tag{29}$$

Considering the joint-velocity limits of the HRMMM $\dot{\boldsymbol{q}}_{\min}$ and $\dot{\boldsymbol{q}}_{\max}$, a unified velocity constraint can be obtained as follows:

$$\boldsymbol{\xi}_{\min} \leqslant \dot{\boldsymbol{q}} \leqslant \boldsymbol{\xi}_{\max}. \tag{30}$$

Here, $\boldsymbol{\xi}_{\min}$ and $\boldsymbol{\xi}_{\max}$ are double-ended constraints, and the ith element can be obtained using the following formula:

$$\left. \begin{array}{l} \xi_{i\,\min} = \max\{\dot{q}_{i\,\min}, \mu(q_{i\,\min} - q_i)\} \\ \xi_{i\,\max} = \min\{\dot{q}_{i\,\max}, \mu(q_{i\,\max} - q_i)\} \end{array} \right\}. \tag{31}$$

2.2.2 Asymmetric-Constraint Transformation

The constraint of the velocity $\dot{\boldsymbol{q}}$ obtained from Eq. (29) is asymmetric. Therefore, it must be changed into a symmetric constraint in order to facilitate the solution of subsequent QP problems. The variable-substitution method was used to transform the asymmetric constraints[30].

With $\dot{q}_i \in [\xi_{i\,\min}, \xi_{i\,\max}]$, $U_{oi} = (\xi_{i\,\max} - \xi_{i\,\min})/2$, $\delta_i = (\xi_{i\,\min} + \xi_{i\,\max})/2$, and $\dot{q}_i = \bar{\dot{q}}_i + \delta_i$, for each control variable:

$$\bar{\dot{q}}_i = \begin{cases} U_{oi}, & \bar{\dot{q}}_i > U_{oi} \\ \bar{\dot{q}}_i, & -U_{oi} \leqslant \bar{\dot{q}}_i \leqslant U_{oi} \\ -U_{oi}, & \bar{\dot{q}}_i < -U_{oi} \end{cases}. \tag{32}$$

The above Eq. (32) transforms the asymmetric variable constraint $[\boldsymbol{\xi}_{\min}, \boldsymbol{\xi}_{\max}]$ into a symmetric constraint $[-\boldsymbol{U}_o, \boldsymbol{U}_o]$. Thus, $\dot{q}_i$ is replaced by a new variable $\bar{\dot{q}}_i$, and an additional constant term δ_i is generated.

The normalization process eliminates the influence of different types of physical variables. The variables in the symmetric constraint system can be easily processed by dividing them by the upper limit of their constraints for normalization, as follows:

$$\bar{\dot{q}}_{\text{norm}} = \frac{\bar{\dot{q}}_i}{U_{oi}}. \tag{33}$$

2.3 Hybrid Motion-Controller Design

After the gripper-tracking velocity $\boldsymbol{V}_g$ was obtained, the required joint velocity was calculated using the inverse kinematics of the manipulator. The kinematic model in Eq. (12) can be directly used to solve the PI of the Jacobian matrix to obtain the joint velocity and then control the manipulator, as follows:

$$\dot{\boldsymbol{q}} = \boldsymbol{J}^+ \boldsymbol{V}_g, \tag{34}$$

where $\boldsymbol{J}^+ = \boldsymbol{J}^{\mathrm{T}}(\boldsymbol{J}\boldsymbol{J}^{\mathrm{T}})^{-1}$ represents the PI of the Jacobian matrix $\boldsymbol{J}$[13]. However, it is difficult to consider complex joint constraints in calculations based on a traditional PI solution. Thus, it is restricted in practical applications.

For a redundant manipulator, the input-constraint saturation is typically considered in the null space, which can be compensated by an anti-saturation function or by using an optimization method. The anti-saturation function of the asymmetric constraints is difficult to design, and the resulting solutions may not be optimal[23]. An optimal solution method can handle the inequality-constraint problem well and ensure that the obtained solution is consistent with the optimal performance index.

Among the many numerical optimal algorithms, QP is considered a rapid constrained optimization algorithm with a small amount of computation[26-27]. However, the optimal problem must be solved within symmetric constraints. Based on the results of Subsection 1.2, QP can be used as an alternative to PI to solve the constrained inverse kinematics of the HRMMM. Therefore, a hybrid control system for the HRMMM was proposed. A logic block diagram of the tracking-control system is shown in Fig. 5.

When the input was not saturated, all joint positions and velocities of the mobile manipulator were within their double-ended constraints, and the PI method was used to solve the inverse kinematics. When saturation occurred, the position or velocity of certain joints could exceed its double-ended constraint. The QP method was used, and the PI solution was taken as the initial condition of the QP to improve the convergence speed.
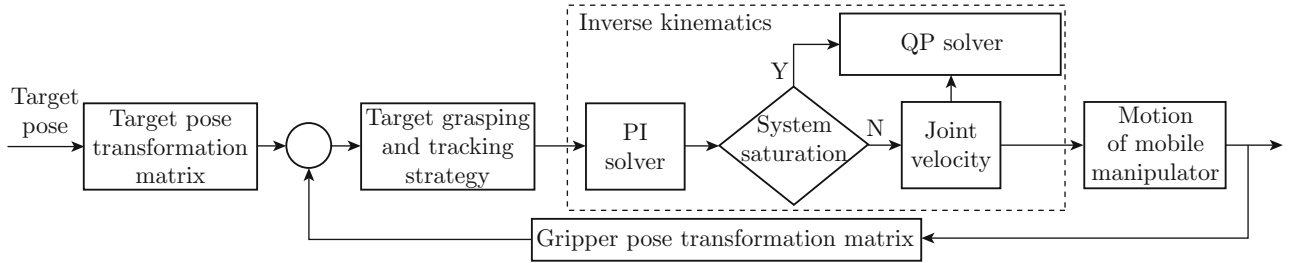
Fig. 5   Tracking control system

A quadratic performance index was designed to ensure smooth switching between the two methods and to ensure that the kinematics was solved within the joint constraints, which could meet the requirements of real-time control.

The performance index of the QP was designed to minimize the change in the joint variables of the HRMMM during the control process to inhibit the switch oscillation of the two controllers. The performance index is as follows:

$$e_{\text{index}} = \min \|\boldsymbol{q} - \boldsymbol{q}_0\|_2^2, \tag{35}$$

where $\boldsymbol{q}$ is the joint variable of the HRMMM at the current moment, and $\boldsymbol{q}_0$ is the joint variable at the previous moment. In addition, the joint-position error function is defined as follows:

$$\hat{\boldsymbol{e}} = \boldsymbol{q} - \boldsymbol{q}_0. \tag{36}$$

According to the exponential-descent convergence principle[31], the time derivative of the tracking control error $\hat{\boldsymbol{e}}$ is

$$\dot{\hat{\boldsymbol{e}}} = \frac{\mathrm{d}\hat{\boldsymbol{e}}}{\mathrm{d}t} = -\lambda(\boldsymbol{q} - \boldsymbol{q}_0). \tag{37}$$

Because the time derivative of Eq. (36) is $\dot{\hat{\boldsymbol{e}}} = \dot{\boldsymbol{q}}$, substituting it into Eq. (37) yields

$$\dot{\boldsymbol{q}} + \lambda(\boldsymbol{q} - \boldsymbol{q}_0) = \boldsymbol{0}. \tag{38}$$

Combining Eq. (38) with the equivalent optimal function Eq. (35) produces the following:

$$\frac{1}{2}(\dot{\boldsymbol{q}} + \lambda(\boldsymbol{q} - \boldsymbol{q}_0))^{\mathrm{T}}(\dot{\boldsymbol{q}} + \lambda(\boldsymbol{q} - \boldsymbol{q}_0)) = \boldsymbol{0}. \tag{39}$$

Then, the variable $\bar{\dot{q}}_i$ in Eq. (32) is substituted into Eq. (39). With $\boldsymbol{c} = \lambda(\boldsymbol{q} - \boldsymbol{q}_0)$, the mathematical model of QP can be obtained as

$$\left.\begin{aligned} \min\ &\frac{1}{2}\bar{\dot{\boldsymbol{q}}}^{\mathrm{T}}\bar{\dot{\boldsymbol{q}}} + (\boldsymbol{c}+\boldsymbol{\delta})^{\mathrm{T}}\bar{\dot{\boldsymbol{q}}} + \frac{1}{2}(\boldsymbol{c}+\boldsymbol{\delta})^{\mathrm{T}}(\boldsymbol{c}+\boldsymbol{\delta}) \\ \text{s.t.}\ &\boldsymbol{J}(\bar{\dot{\boldsymbol{q}}}+\boldsymbol{\delta}) = \boldsymbol{b} \\ &-\boldsymbol{U}_{\mathrm{o}} \leqslant \bar{\dot{\boldsymbol{q}}} \leqslant \boldsymbol{U}_{\mathrm{o}} \end{aligned}\right\}, \tag{40}$$

where $\frac{1}{2}(\boldsymbol{c}+\boldsymbol{\delta})^{\mathrm{T}}(\boldsymbol{c}+\boldsymbol{\delta})$ is a nonnegative term that does not affect the results. Thus, after the equation is normalized in accordance with Eq. (33), the QP optimization scheme is described as follows:

$$\left.\begin{aligned} \min\ &\frac{1}{2}\bar{\dot{\boldsymbol{q}}}^{\mathrm{T}}\boldsymbol{H}\bar{\dot{\boldsymbol{q}}} + \boldsymbol{f}^{\mathrm{T}}\bar{\dot{\boldsymbol{q}}} \\ \text{s.t.}\ &\boldsymbol{J}\bar{\dot{\boldsymbol{q}}} = \boldsymbol{b} - \boldsymbol{J}\boldsymbol{\delta} \\ &-\boldsymbol{U}_{\mathrm{o}} \leqslant \bar{\dot{\boldsymbol{q}}} \leqslant \boldsymbol{U}_{\mathrm{o}} \end{aligned}\right\}, \tag{41}$$

where $\bar{\dot{\boldsymbol{q}}} = \dot{\boldsymbol{q}} - \boldsymbol{\delta} \in \mathbb{R}^n$ is the variable to be solved, $\boldsymbol{b} \in \mathbb{R}^m$ represents the generalized velocity at the end of the HRMMM, $\boldsymbol{J} \in \mathbb{R}^{m \times n}$ is the Jacobian matrix, and $\boldsymbol{f} = \boldsymbol{D}(\boldsymbol{c} + \boldsymbol{\delta}) \in \mathbb{R}^n$ is the coefficient vector. In addition, $\boldsymbol{H} \in \mathbb{R}^{n \times n}$ is the coefficient matrix, which can be designed as follows:

$$\boldsymbol{H} = \boldsymbol{D}^{\mathrm{T}}\boldsymbol{D}, \tag{42}$$

where, $\boldsymbol{D} = \mathrm{diag}\left(\dfrac{1}{\boldsymbol{U}_{\mathrm{o}}}\right) \in \mathbb{R}^{n \times n}$ denotes the normalized matrix.

3   Medical-Application Example

In the context of the COVID-19 pandemic, the medical staff working in the isolation area are at risk of infection. The HRMMM could help medical staff deliver or retrieve items, thereby effectively reducing the risk of exposure to COVID-19 or other biological hazards.

3.1   Pose-Tracking Results

To meet the physical constraints, this section provides the simulation results of target tracking based on a hybrid control algorithm with an individual QP for comparison. Figure 6(a) illustrates an experimental situation in which the HRMMM moves with a given bottle from an initial pose and throws it into a rubbish bin with the target pose.

The initial joint state of the HRMMM is

$$\begin{aligned} \boldsymbol{q} = (&0, 0, 0, 3.14\,\text{rad}, -1.386\,\text{rad}, 0, -2.086\,\text{rad}, 0, \\ &1.756\,\text{rad}, 1.571\,\text{rad})^{\mathrm{T}}. \end{aligned}$$

Furthermore, the initial pose is deduced from the forward kinematics:

$$\begin{aligned} \boldsymbol{p}_{\mathrm{e}} = (&0.675\,\text{m}, 0.024\,6\,\text{m}, 0.856\,\text{m}, 1.716\,\text{rad}, \\ &0, 1.571\,\text{rad})^{\mathrm{T}}, \end{aligned}$$

(a) Experimental situation

(b) Gripper position

(c) Gripper attitude

—— Hybrid algorithm, ---- QP algorithm, • Initial, ☆ Target
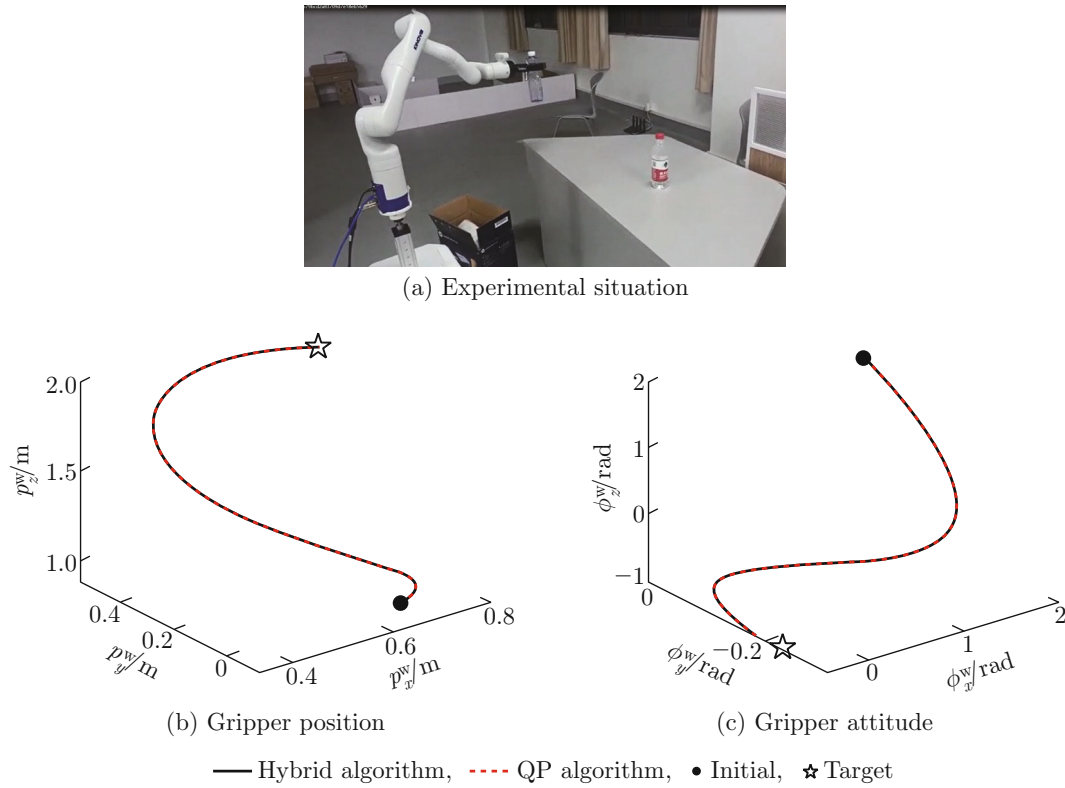
Fig. 6   Tracking trajectories

and the target pose is set as

$$\boldsymbol{p}_{*\mathrm{e}} = (0.8\,\mathrm{m}, 0.5\,\mathrm{m}, 1.843\,\mathrm{m}, -0.426\,\mathrm{rad}, -0.227\,\mathrm{rad}, \\ -0.971\,\mathrm{rad})^{\mathrm{T}}.$$

The control period is 0.1 s, and the other design parameters of the tracking controller are $\mu = 10$, $\lambda = 0.2$, and $k = 0.2$. The termination condition of the algorithm was set as the modulus of the final target-pose error vector; that is, $\|\boldsymbol{e}\| < 0.05$.

The tracking trajectories of the two algorithms are shown in Figs. 6(b) and 6(c). Figure 6(b) shows the trajectory of the gripper position, and Fig. 6(c) shows the trajectory of the gripper attitude expressed by the Euler angles. The hybrid and QP methods obtained similar position and attitude tracking results, owing to the same pose-tracking strategy.

After the tracking was completed, the moduli of the position and attitude errors of the gripper were found to be 0.015 and 0.047, respectively. The tracking results for the target object were satisfactory and the motion trajectory at the end of the manipulator was smooth and stable.

The joint-position variations of the two algorithms are compared in Fig. 7. The double-ended position constraints of Joints 2, 4, and 6 and the vertical displacement d in the tracking process are shown in Figs. 7(b), 7(d), 7(f), and 7(h), respectively.   Joint 4 reached

$-2.548\,7\,\mathrm{rad}$ at 1.7 s, which is close to its position limit of $-2.58\,\mathrm{rad}$. The final values of the two algorithms stabilized at $-1.562\,\mathrm{rad}$ and $-1.312\,\mathrm{rad}$, respectively. Joint 6 reached its limit position of 2.1 rad at 2.7 s and lasted till 3.4 s, but gradually left the limit position. The final values of the two algorithms stabilized at 2.065 rad and 1.855 rad, respectively.

The joint-velocity variations in the HRMMM are shown in Fig. 8. The double-ended velocity constraints of all the joints are described. Joints 3 and 4 reached their maximum of 1.39 rad/s at 2.6 s, as shown in Figs. 8(c) and 8(d). However, they quickly withdrew from the saturation state and finally stabilized at approximately 0 rad/s. Joint 4 reached 0.084 7 rad/s at 1.7 s, and its joint position was close to the lower limit around 1.7 s (Fig. 7(d)).

Joint 6 was at the upper limit of the joint-velocity constraint from 2.5 s to 3.4 s, but it gradually withdrew from the limit and stabilized at around 0 rad/s. Joint 7 reached 1.1771 rad/s at 1.8 s, which is close to its upper limit of 1.22 rad/s, and finally stabilized at around 0 rad/s (Fig. 8(g)). The other joint velocities are far from their limits.

Figures 8(d) and 8(f) show that the double-ended velocity constraint of joint 4 is asymmetric because it is related to the current joint positions, as described in Eq. (31). The upper limits of the two algorithms of joint 6 are inconsistent from 4.3 s, as shown in Fig. 8(f),
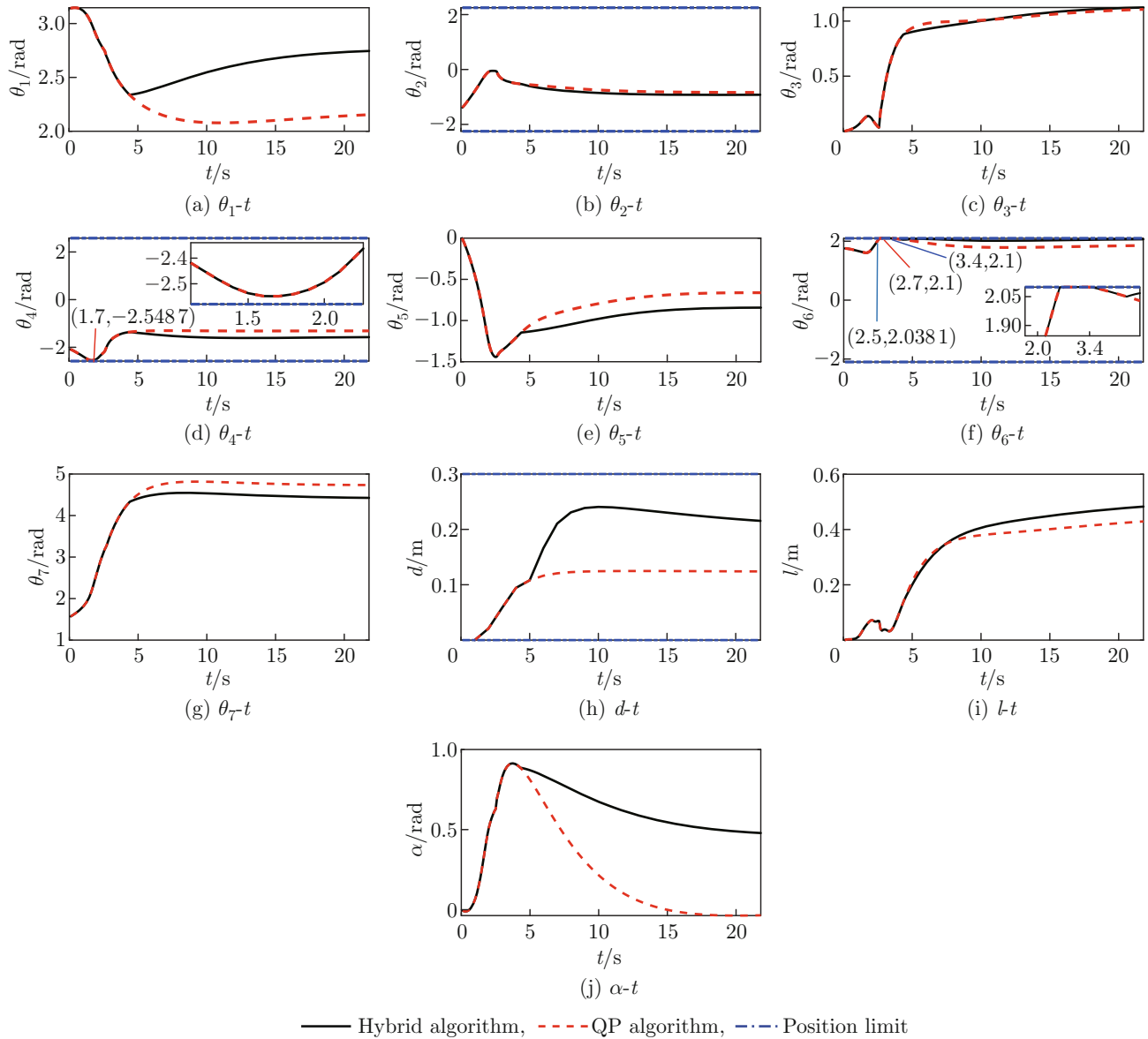
Fig. 7   HRMMM positions

because the hybrid control switches to PI from 4.3 s (Fig. 9(b)). Thus, the solution of the hybrid is different from that of QP, similar to the joint-velocity limits. The vertical velocity of the manipulator reaches its limit of 0.1 m/s at 2.6 s, as shown in Fig. 8(h).

The simulation results in Figs. 7 and 8 prove that all the joint positions and velocities of the HRMMM are within their limit constraints; that is, both methods can effectively satisfy input constraints of different types and levels.

3.2   Computational-Efficiency Analysis

The computer processor used in the simulation is a 2.50 GHz Intel Core$^{\text{TM}}$ i5-7300HQ CPU with 16 GB of memory. The CPU calculation time for the two algorithms is shown in Fig. 9(a). In this simulation, the CPU calculation time of the hybrid algorithm is much

shorter than that of the QP algorithm.

Two other target poses are selected to verify the computational advantages of the hybrid algorithm over the QP algorithm. Each target pose is traced ten times, and the average CPU calculation time is calculated. The calculation results for the two algorithms are presented in Table 1. The average CPU calculation time of the hybrid algorithm is one-third that of QP.

The switching flag of the two solution schemes in the hybrid algorithm is shown in Fig. 9(b). Owing to the large pose error at the initial tracking stage, the physical constraint of the HRMMM reaches saturation, and the hybrid algorithm chooses QP to solve the inverse kinematics. Thus, the simulation results are the same as those of the QP algorithm.

From 4.3 s, all joints of the system withdrew from
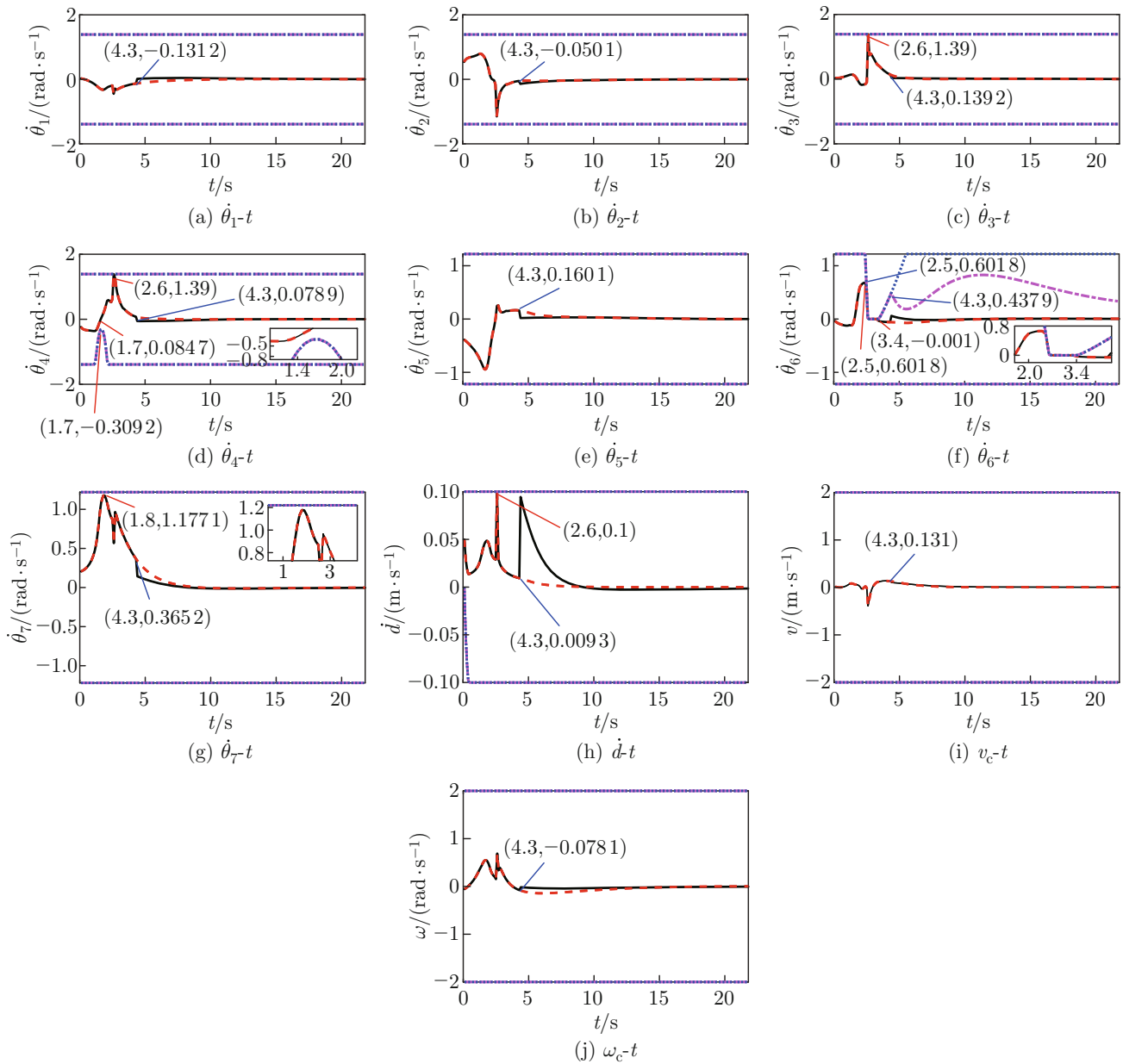
Fig. 8   HRMMM velocities

Table 1   Calculation-time comparison

Target pose	CPU time/s	
	QP	Hybrid
$(0.8\,\text{m}, 0.5\,\text{m}, 1.843\,\text{m}, -0.426\,\text{rad}, -0.227\,\text{rad}, -0.971\,\text{rad})^{\text{T}}$	2.469	0.802
$(0.8\,\text{m}, 0.5\,\text{m}, 1.843\,\text{m}, -0.597\,\text{rad}, -0.058\,1\,\text{rad}, -0.188\,\text{rad})^{\text{T}}$	2.393	0.884
$(0.7\,\text{m}, 0.5\,\text{m}, 1.7\,\text{m}, -0.426\,\text{rad}, -0.227\,\text{rad}, -0.971\,\text{rad})^{\text{T}}$	2.428	0.766

saturation, and the hybrid control system switched to PI for the inverse kinematic calculation. An evident switching oscillation can be observed in the vertical velocity, as shown in Fig. 8(h). However, no obvious switching oscillation of the joint position was observed, as shown in Fig. 7. Thus, the performance index performed well in suppressing the switching oscillation.

The performance index is a quadratic function of

(a) CPU calculation time (b) Switch flag in hybrid control (c) Performance index
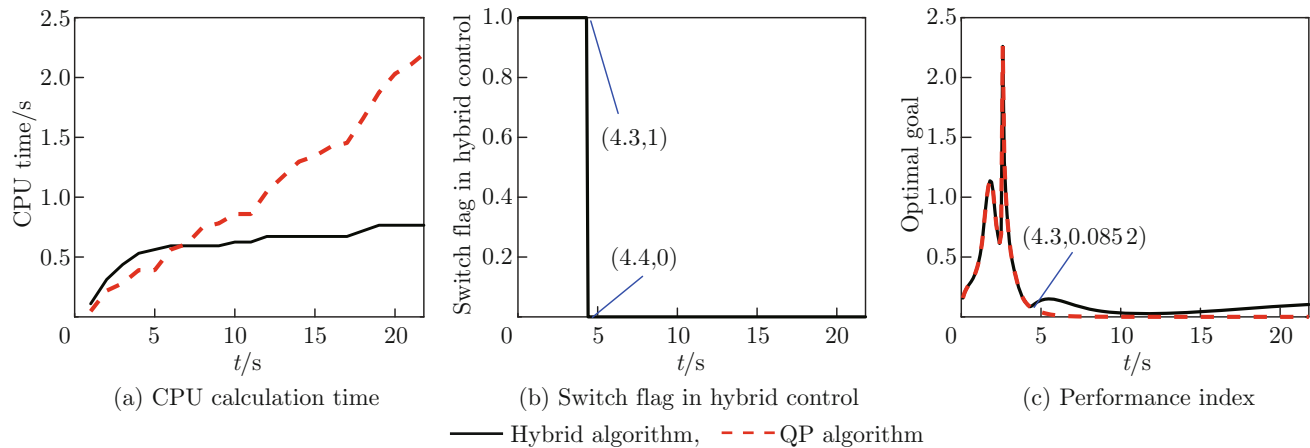
—— Hybrid algorithm, - - - QP algorithm

Fig. 9   Controller states

the joint-position variation representing the energy consumption. The performances of the two algorithms are shown in Fig. 9(c). The function values of the two algorithms were essentially the same in the initial stage because they both used the QP method. Moreover, the function value of the hybrid algorithm was slightly larger than that of QP when reaching saturation (at 4.3 s), but without a significant difference.

In the entire control process, the system spends only a small amount of time in saturation. Therefore, it is not necessary to use an optimization algorithm to solve the inverse kinematics, thereby proving the superiority of the hybrid algorithm.

4   Conclusion

The anti-saturation tracking control algorithm based on hybrid optimization ensured that the HRMMM completed the target tracking within the joint physical constraints, which is important for real applications. The variable-substitution method was used to transform asymmetric constraints into symmetric constraints. A quadratic performance index was designed to ensure smooth switching between the two hybrid controller algorithms. The hybrid algorithm proposed in this study was the same as QP, in terms of tracking performance and energy consumption. However, its computational efficiency was significantly improved.

The limitation of the proposed hybrid control algorithm is that the acceleration constraints are not considered. Future research should include dynamic control for safe force interactions in medical applications.

References

[1] ZHANG W, LI H, CUI L, et al. Research progress and development trend of surgical robot and surgical instrument arm [J]. *The International Journal of Medical Robotics and Computer Assisted Surgery*, 2021, **17**(5): e2309.

[2] MAYETIN U, KUCUK S. A low cost 3-DOF force sensing unit design for wrist rehabilitation robots [J]. *Mechatronics*, 2021, **78**: 102623.

[3] PETERS B S, ARMIJO P R, KRAUSE C, et al. Review of emerging surgical robotic technology [J]. *Surgical Endoscopy*, 2018, **32**(4): 1636-1655.

[4] ZHAO F, YANG Z, LI X, et al. Extract executable action sequences from natural language instructions based on DQN for medical service robots [J]. *International Journal of Computers Communications & Control*, 2021, **16**(2): 4115.

[5] LI Z, MORAN P, DONG Q, et al. Development of a tele-nursing mobile manipulator for remote caregiving in quarantine areas [C]//*2017 IEEE International Conference on Robotics and Automation*. Singapore: IEEE, 2017: 3581-3586.

[6] BOSTELMAN R, HONG T, MARVEL J. Survey of research for performance measurement of mobile manipulators [J]. *Journal of Research of the National Institute of Standards and Technology*, 2016, **121**: 342-366.

[7] MATHEW S S, JISHA V R. Decentralized control of a slow moving mobile manipulator [C]//*2022 IEEE International Conference on Signal Processing, Informatics, Communication and Energy Systems*. Thiruvananthapuram: IEEE, 2022: 442-447.

[8] EGERSTEDT N, HU X. Coordinated trajectory following for mobile manipulation [C]//*Proceedings 2000 ICRA. Millennium Conference. IEEE International Conference on Robotics and Automation. Symposia Proceedings*. San Francisco: IEEE, 2000: 3479-3484.

[9] YAMAMOTO Y, YUN X. Coordinating locomotion and manipulation of a mobile manipulator [J]. *IEEE Transactions on Automatic Control*, 1994, **39**(6): 1326-1332.

[10] HUANG Q, TANIE K, SUGANO S. Coordinated motion planning for a mobile manipulator considering stability and manipulation [J]. *The International Journal of Robotics Research*, 2000, **19**(8): 732-742.

[11] KORAYEM M H, ESFEDEN R A, NEKOO S R. Path planning algorithm in wheeled mobile manipulators

based on motion of arms [J]. *Journal of Mechanical Science and Technology*, 2015, **29**(4): 1753-1763.

[12] SERAJI H. A unified approach to motion control of mobile manipulators [J]. *The International Journal of Robotics Research*, 1998, **17**(2): 107-118.

[13] LI W, XIONG R. A hybrid visual servo control method for simultaneously controlling a nonholonomic mobile and a manipulator [J]. *Frontiers of Information Technology & Electronic Engineering*, 2021, **22**(2): 141-154.

[14] GIFTTHALER M, FARSHIDIAN F, SANDY T, et al. Efficient kinematic planning for mobile manipulators with non-holonomic constraints using optimal control [C]//*2017 IEEE International Conference on Robotics and Automation*. Singapore: IEEE, 2017: 3411-3417.

[15] BUSS S R, KIM J S. Selectively damped least squares for inverse kinematics [J]. *Journal of Graphics Tools*, 2005, **10**(3): 37-49.

[16] ZHANG X, FAN B, WANG C, et al. An improved weighted gradient projection method for inverse kinematics of redundant surgical manipulators [J]. *Sensors*, 2021, **21**(21): 7362.

[17] CHAN T F, DUBEY R V. A weighted least-norm solution based scheme for avoiding joint limits for redundant manipulators [C]//*IEEE International Conference on Robotics and Automation*. Atlanta: IEEE, 1993: 395-402.

[18] WAN J, WU H T, MA R, et al. A study on avoiding joint limits for inverse kinematics of redundant manipulators using improved clamping weighted least-norm method [J]. *Journal of Mechanical Science and Technology*, 2018, **32**(3): 1367-1378.

[19] TOSHANI H, FARROKHI M. Real-time inverse kinematics of redundant manipulators using neural networks and quadratic programming: A Lyapunov-based approach [J]. *Robotics and Autonomous Systems*, 2014, **62**(6): 766-781.

[20] ZHANG Z, CHEN S, ZHU X, et al. Two hybrid end-effector posture-maintaining and obstacle-limits avoidance schemes for redundant robot manipulators [J]. *IEEE Transactions on Industrial Informatics*, 2020, **16**(2): 754-763.

[21] KELEMEN M, VIRGALA I, LIPTÁK T, et al. A novel approach for a inverse kinematics solution of a redundant manipulator [J]. *Applied Sciences*, 2018, **8**(11): 2229.

[22] FARONI M, BESCHI M, PEDROCCHI N, et al. Predictive inverse kinematics for redundant manipulators with task scaling and kinematic constraints [J]. *IEEE Transactions on Robotics*, 2019, **35**(1): 278-285.

[23] FLACCO F, DE LUCA A, KHATIB O. Control of redundant robots under hard joint constraints: Saturation in the null space [J]. *IEEE Transactions on Robotics*, 2015, **31**(3): 637-654.

[24] KIM K, NA M, SONG J B. Joint limit avoidance of a mobile manipulator for prevention of rapid velocity increase [C]//*2021 18th International Conference on Ubiquitous Robots*. Gangneung: IEEE, 2021: 244-248.

[25] LEORO J, HSIAO T. Motion planning of nonholonomic mobile manipulators with manipulability maximization considering joints physical constraints and self-collision avoidance [J]. *Applied Sciences*, 2021, **11**(14): 6509.

[26] QUIROZ-OMAÑA J J, ADORNO B V. Whole-body kinematic control of nonholonomic mobile manipulators using linear programming [J]. *Journal of Intelligent & Robotic Systems*, 2018, **91**(2): 263-278.

[27] ZHANG Z J, CHEN S Y, XIE J H, et al. Two hybrid multiobjective motion planning schemes synthesized by recurrent neural networks for wheeled mobile robot manipulators [J]. *IEEE Transactions on Systems, Man, and Cybernetics*: *Systems*, 2021, **51**(5): 3270-3281.

[28] GALLEGO G, YEZZI A. A compact formula for the derivative of a 3-D rotation in exponential coordinates [J]. *Journal of Mathematical Imaging and Vision*, 2015, **51**(3): 378-384.

[29] YU Y, DING X, ZHU J J. Attitude tracking control of a quadrotor UAV in the exponential coordinates [J]. *Journal of the Franklin Institute*, 2013, **350**(8): 2044-2068.

[30] BENZAOUIA A, BENHAYOUN M, MESQUINE F. Stabilization of systems with unsymmetrical saturated control: An LMI approach [J]. *Circuits, Systems, and Signal Processing*, 2014, **33**(10): 3263-3275.

[31] LI K, ZHANG Y. State adjustment of redundant robot manipulator based on quadratic programming [J]. *Robotica*, 2012, **30**(3): 477-489.